Chemical Science

ROYAL SOCIETY OF CHEMISTRY

EDGE ARTICLE

View Article Online
View Journal | View Issue



Cite this: *Chem. Sci.*, 2024, **15**, 17562

All publication charges for this article have been paid for by the Royal Society of Chemistry

Received 29th July 2024
Accepted 1st October 2024

DOI: 10.1039/d4sc05053c

rsc.li/chemical-science

# Systematic design and functionalisation of amorphous zirconium metal–organic frameworks†

Nattapol Ma, *[ab] Soracha Kosasang, [c] Jennifer Theissen, [a] Nick Gys, [ad] Tom Hauffman,[d] Ken-ichi Otake, [e] Satoshi Horike [cef] and Rob Ameloot *[a]

Controlling the structure and functionality of crystalline metal–organic frameworks (MOFs) using molecular building units and post-synthetic functionalisation presents challenges when extending this approach to their amorphous counterparts (aMOFs). Here, we present a new bottom-up approach for synthesising a series of Zr-based aMOFs, which involves linking metal–organic clusters with specific ligands to regulate local connectivity. In addition, we overcome the limitations of post-synthetic modifications in amorphous systems, demonstrating that homogeneous functionalisation is achievable even without regular internal voids. By altering the acidity of the side group, length, and degree of connectivity of the linker, we could control the porosity, proton conductivity, and mechanical properties of the resulting aMOFs.

## Introduction

The directionality of coordination bonding enables predictable and precise positioning of atomic arrangements in three-dimensional space,[1,2] enabling the design of crystalline metal–organic frameworks (MOFs) by selecting appropriate metal ion and multitopic organic ligand building units.[3–9] Additional chemical functionalisation of assembled MOFs is also feasible through post-synthetic modifications.[10,11] The recent emergence of amorphous MOFs (aMOFs), some showing glass transition,[12–14] presents unique or complementary properties, including improved ion mobility, transparency, and processability.[15–20]

Typically, aMOFs are synthesised in crystalline form and subsequently amorphised by melt-quenching,[15,21] dehydration or desolvation,[22,23] mechanical milling,[24] pressure,[25,26] or radiation.[27] Nevertheless, these approaches can only be applied when the MOFs are stable during amorphisation. In practice, the majority of materials are prone to organic linker decomposition. Additionally, controlling their properties and local structure poses a challenge, given their top-down preparation[14] and since post-synthetic modification is typically confined to the outer surface due to the absence of regular pores.[28]

This article presents a bottom-up strategy for designing a series of zirconium-based aMOFs. The approach uses predefined zirconium oxo clusters ($Zr_6$) cross-linked with a selection of flexible ligands (Fig. 1). Analysis of the local structures revealed the preservation of the $Zr_6$ cluster units. Post-synthetic modification is showcased in the gel phase before densification, resulting in homogeneous functionalisation with sulfonic acid groups. The presented strategy shows how the porosity, proton conductivity, and mechanical properties of the formed aMOFs can be systematically controlled *via* the presence of the side group, ligand length, and degree of connectivity.

## Results and discussion

### Sol–gel synthesis of cross-linked Zr clusters

Water-soluble $Zr_6$ oxo cluster, $Zr_6O_4(OH)_4(H_2O)_8(CH_3COO)_8Cl_4$, denoted as ZrOAc, was synthesised as reported, and its formation was confirmed by powder X-ray diffraction (PXRD), Fourier transform infrared (FTIR), and thermal gravimetric analysis (TGA) (Fig. S1–S3†).[29] We selected three flexible aliphatic bidentate ligands—succinic acid ($L_1$), adipic acid ($L_2$), and thiomalic acid ($L_3$)—to prevent the formation of crystalline products (Fig. 1). The ZrOAc clusters were cross-linked by adding 2, 4, 8, and 12 molar equivalents of aqueous solutions of ligand (*n*

[a]*Centre for Membrane Separations, Adsorption, Catalysis, and Spectroscopy (cMACS), KU Leuven, Celestijnenlaan 200F, 3001 Leuven, Belgium. E-mail: rob.ameloot@kuleuven.be*

[b]*International Center for Young Scientists (ICYS), National Institute for Materials Science, 1-1 Namiki, Tsukuba, Ibaraki, 305-0044, Japan. E-mail: ma.nattapol@nims.go.jp*

[c]*Department of Chemistry, Graduate School of Science, Kyoto University, Kitashirakawa-oiwake-cho, Sakyo-ku, Kyoto 606-8502, Japan*

[d]*Sustainable Materials Engineering (SUME) Research Group of Electrochemical and Surface Engineering (SURF), Depart-ment of Materials and Chemistry, Vrije Universiteit Brussel, Pleinlaan 2, Brussels 1050, Belgium*

[e]*Institute for Integrated Cell-Material Sciences, Institute for Advanced Study, Kyoto University, Yoshida-Honmachi, Sakyo-ku, Kyoto 606-8501, Japan*

[f]*Department of Materials Science and Engineering, School of Molecular Science and Engineering, Vidyasirimedhi Institute of Science and Technology, Rayong, 21210, Thailand*

† Electronic supplementary information (ESI) available. See DOI: https://doi.org/10.1039/d4sc05053c

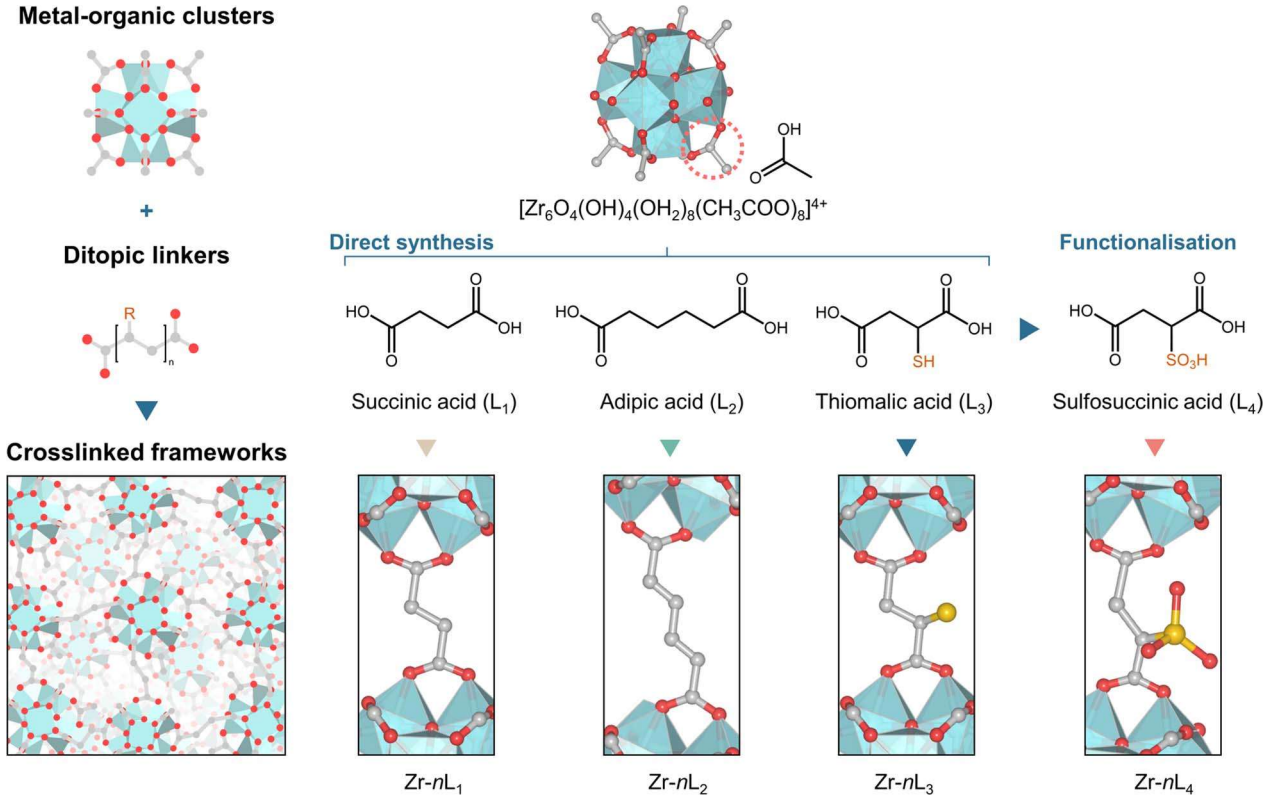


Fig. 1 Schematic overview of the synthesis routes and functionalisation of zirconium-based amorphous metal–organic frameworks (aMOFs). The Zr–$n$L$_1$, Zr–$n$L$_2$, and Zr–$n$L$_3$ aMOFs are synthesised by pairing the $Zr_6O_4(OH)_4(H_2O)_8(CH_3COO)_8Cl_4$ (ZrOAc) cluster with three bidentate ligands, including succinic acid (L$_1$), adipic acid (L$_2$), and thiomalic acid (L$_3$). Post-synthetic modification of a cross-linked Zr–$n$L$_3$ in the gel phase provides Zr–$n$L$_4$ frameworks with sulfosuccinate (L$_4$). Zr, O, C, and S atoms are represented by light blue, red, grey, and yellow spheres, respectively. H atoms are omitted for clarity.

ratio) to ZrOAc, followed by heating at 80 °C for 72 h. The process resulted in the formation of gels (Fig. S4†).[30–35] Considering that all starting components are highly soluble in water, the distinct change in solubility suggests the cross-linking of ZrOAc clusters.[36] For L$_1$ and L$_2$, the minimum $n$ ratio required to initiate gelation is 4, while $n = 2$ is sufficient for L$_3$. The gels were then washed and dried at 60 °C for 72 h. The resulting aMOFs are referred to as Zr–$n$L$_x$, where $n$ represents the molar equivalent of ligands (L$_x$ = L$_1$, L$_2$, or L$_3$) used during cross-linking. The amorphous nature of all samples was confirmed by the board diffuse scattering patterns observed by laboratory (Fig. S5–S7†) and synchrotron PXRD (Fig. 2A). Optical images of Zr–$n$L$_1$ samples show transparent, glass-like monolith, while Zr–$n$L$_2$ and Zr–$n$L$_3$ became more opaque at higher linker ratios (Fig. 2B and S8–S10†). Scanning electron microscopy (SEM) images of as-synthesised Zr–4L$_1$, Zr–4L$_2$, and Zr–4L$_3$ samples revealed smooth surfaces without any trace of distinguishable microparticles (Fig. S11–S13†). Based on TGA data under $N_2$ flow before and after dehydration at 200 °C (Fig. S14–S23†), the interstitial water contents were determined at 10.0–15.2 wt%. Additionally, all cross-linked compounds were found to be thermally stable up to at least 220 °C.

The incorporation of the ligands was confirmed by FTIR and $^1$H NMR (Fig. 2C and S24–S37†), with ethanol residue detected in Zr–$n$L$_2$ and Zr–$n$L$_3$. FTIR Peaks at 2926–2936, 1300–1306, and 1153–1173 cm$^{-1}$ were assigned to the $\nu$(CH), $\tau$(CH$_2$), and $\tau$(CH$_2$) vibrations of succinate.[39,40] In Zr–$n$L$_2$, an additional $\nu$(CH) band appeared around 2864–2871 cm$^{-1}$, corresponding to longer aliphatic chain units. For Zr–$n$L$_3$, a peak associated with the S–H bond was identified at 2556–2561 cm$^{-1}$.[41] Additionally, the presence of C=O stretching at 1690–1730 cm$^{-1}$ suggests the coexistence of non-coordinating carboxylate or carboxylic acid arising from monodentate ligands.[42] When $n = 4$, the ratios of incorporated bidentate ligands and acetate were comparable for L$_1$, L$_2$, and L$_3$ (Fig. S38†). Consequently, Zr–4L$_1$, Zr–4L$_2$, and Zr–4L$_3$ were selected for further characterization. The TGA analysis under air indicated the presence of linker vacancies, revealing the ratios between bidentate ligands and Zr$_6$ clusters in Zr–4L$_1$, Zr–4L$_2$, and Zr–4L$_3$ to be 3.5, 4.3, and 3.7 instead of 6 for full cross-linking (Fig. S39†).[43]

The thermal behaviour of dehydrated Zr–4L$_1$, Zr–4L$_2$, and Zr–4L$_3$ was further investigated using differential scanning calorimetry (DSC, Fig. S40†).[44] All samples exhibit an endothermic baseline shift between 104.4 and 112.7 °C at a heating rate of 10 °C min$^{-1}$. However, these baseline shifts are smaller than previously reported values. For example, the measured change in heat capacity ($\Delta C_p$) of Zr–4L$_1$, using sapphire reference, is 0.013 J g$^{-1}$ °C$^{-1}$ (Fig. S41†), which is significantly lower than the $\Delta C_p$ associated with the glass transition temperature in other

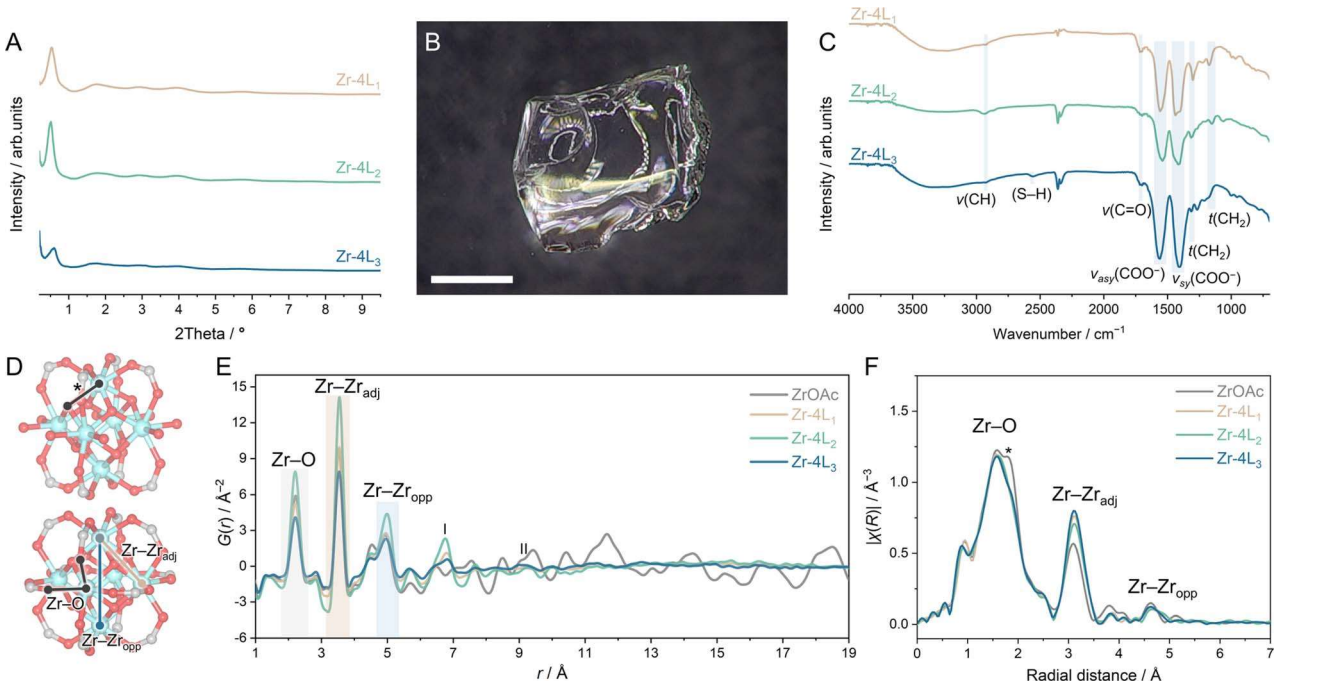


Fig. 2 Sol–gel synthesis of cross-linked zirconium-based aMOFs. (A) Synchrotron PXRD ($\lambda$ = 0.109795 Å) of Zr–4L$_1$, Zr–4L$_2$, and Zr–4L$_3$. (B) Optical image of the as-synthesised Zr–4L$_1$. Scale bar = 0.5 mm. (C) FTIR spectra of Zr–4L$_1$, Zr–4L$_2$, and Zr–4L$_3$. (D) Zr-cluster model representations for (E and F) peak assignments. The structures are determined from single crystal data of (top) $[Zr_6O_4(OH)_4(H_2O)_8(Gly)_8]\cdot 12Cl\cdot 8H_2O$[37] and (bottom) $[Zr_6O_4(OH)_4(CH_3COO)_{12}]\cdot 8.5H_2O$.[38] Zr, C, and O atoms are represented by light blue, grey, and red, respectively. The longer Zr–$\mu_3$-O pair distance in the trigonal zirconium plane is marked with an asterisk. (E) Pair distribution function (PDF) and (F) extended X-ray absorption fine structure (EXAFS) at the Zr-K edge of ZrOAc, Zr–4L$_1$, Zr–4L$_2$, and Zr–4L$_3$.

MOF and coordination polymer glasses, such as 0.16 J g$^{-1}$ °C$^{-1}$ in ZIF-4 or 0.34 J g$^{-1}$ °C$^{-1}$ in $[CsHSO_4]_{0.5}[ZnPIm]_{0.5}$ glasses.[45,46]

## Chemical structures and short-range ordering

Using synchrotron X-ray total scattering, we characterised the short-range ordering within Zr–4L$_1$, Zr–4L$_2$, and Zr–4L$_3$. The Fourier transformation and the Lorch modification of the Faber–Ziman total structure factor, $S(Q)$, were employed to obtain atomic pair information represented as pair distribution functions (PDFs, Fig. 2D and E).[47–49] The peak features of Zr–4L$_1$, Zr–4L$_2$, and Zr–4L$_3$ closely resemble those of the pristine ZrOAc cluster up to 5.0 Å. The range includes the retention of Zr–O bonds (2.2 Å), Zr⋯Zr correlations of the adjacent site (Zr–Zr$_{adj}$, 3.5 Å), and Zr⋯Zr correlations of the opposite site (Zr–Zr$_{opp}$, 5.0 Å). These observations confirm that the Zr$_6$ building unit is maintained in all aMOFs.

The peak between 6.5 and 6.8 Å (Fig. 2E, labelled with I) in Zr–4L$_1$, Zr–4L$_2$, and Zr–4L$_3$ corresponds to the distance between $Zr^{4+}$ and the fourth neighbour C atoms of the stretched bridging ligand and opposite carboxylate O atoms that link the nearby cluster. The pair distance closely aligns with the Zr⋯C (6.4–7.0 Å) and Zr⋯O of the carboxylate (6.9–7.1 Å) observed in Zr-MOFs comprising fumarate or aspartate ligands.[50,51] To support the peak assignments, we conducted additional X-ray total scattering and PDF analysis on two crystalline MOFs with Zr$_6$ units, MOF-801 and UiO-66 (Fig. S43†), together with a partial PDF simulation for MOF-801 (Fig. S44†). Above 7 Å, the PDF profiles of Zr–4L$_1$, Zr–4L$_2$, and Zr–4L$_3$ show less intense and broader peaks, reflecting the diminishing periodicity characteristic of their amorphous nature.[52] The peak labelled II in Fig. 2E is the expected position for inter-cluster Zr⋯Zr correlations for Zr–4L$_1$ and Zr–4L$_3$. For Zr–4L$_2$, the same correlation is expected around 9–12 Å due to a wide conformational arrangement of the adipate linker.[40,53]

The local coordination environments of the Zr$_6$ clusters before and after cross-linking were examined using Fourier-transform (FT) Zr K-edge extended X-ray absorption fine structure (EXAFS, Fig. 2F).[38] The main characteristic peaks for Zr$_6$ units at *ca.* 1.58, 3.10, and 4.64 Å, corresponding to the radial distances of Zr–O, Zr–Zr$_{adj}$, and Zr–Zr$_{opp}$ pairs (Fig. 2D), are observed in all samples: ZrOAc, Zr–4L$_1$, Zr–4L$_2$, and Zr–4L$_3$. The peak assignments were confirmed by EXAFS fitting for Zr–4L$_1$, Zr–4L$_2$, and Zr–4L$_3$ using the $Zr_6(O)_4(OH)_4(CH_3COO)_{12}\cdot 8.5H_2O$[38] crystal structure as a model (Fig. S47 and Table S1†). The fitted Zr–Zr distances of 3.54–3.55 Å align well with the pair distances observed in PDF analysis. Apart from the ligand types, the local environments of Zr–4L$_1$, Zr–4L$_2$, and Zr–4L$_3$ are indistinguishable. When comparing the ZrOAc building unit with the cross-linked frameworks, an additional peak at *ca.* 1.80 Å only observed for ZrOAc is attributed to longer Zr–$\mu_3$-O linkages in the trigonal zirconium plane. The identical elongation of the Zr–O bond is also observed in other Zr$_6$ clusters with 8 bidentate bridging carboxylate coordination, such as $[Zr_6(O)_4(OH)_4(H_2O)_8(Gly)_8]\cdot 12Cl\cdot 8H_2O$ and

$[Zr_6(OH)_8(H_2O)_8(HGly)_4(Gly)_4]\cdot(SO_4)_6\cdot 14H_2O$ (HGly = protonated glycine), where the equatorial edges of both clusters are not coordinated by glycine ligand but are instead capped with 8 water molecules (Fig. S48†).[37,54] This Zr–O bond elongation, however, is absent in the 12-coordinated $Zr_6$ cluster, such as $Zr_6(O)_4(OH)_4(CH_3COO)_{12}\cdot 8.5H_2O$,[38] or in defective $Zr_6$ clusters capped with water or hydroxide molecules in irregular positions.[55] These results suggest that cross-linking occurs in an alternate position and differs from the regular 8-coordination in the starting $Zr_6$ cluster (ZrOAc).

The change in oxidation state and chemical environment was probed by X-ray photoelectron spectroscopy (XPS). The presence of $Cl^-$ in ZrOAc (267 and 196 eV) further emphasises that the $Zr_6$ cluster comprises 8 coordinated water molecules, as counter anions are necessary to compensate for the overall charge balance requirements (Fig. S49†).[37,54] This is not the case for Zr–4$L_1$, Zr–4$L_2$, and Zr–4$L_3$, since $Cl^-$ are eliminated after the cross-linking process and the charge neutrality should be maintained by hydroxide anions (Fig. S50–S52†).[55] XPS further confirms the presence of the S atom in Zr–4$L_3$ (Fig. S52†), and XPS at the Zr 3d region remains identical to ZrOAc, indicating the retention of the $Zr^{4+}$ oxidation state for all samples (Fig. S53–S56†).

## Post-synthetic modification

The absence of regular internal voids in aMOF usually impedes the diffusion of reactants, resulting in inhomogeneous functionalisation. To circumvent this limitation, we conducted post-synthetic modifications in the gel phase (Fig. 3A). Oxidation of thiols (–SH) to sulfonic acid groups (–$SO_3H$) was achieved by soaking Zr–*n*$L_3$ gels in a 35% $H_2O_2$ solution for 2 h.[41,57] The resulting material was washed with deionised water, and protonation was completed with 0.02 M $H_2SO_4$ (see ESI†). Subsequently, the protonated gels underwent further washing cycles, solvent exchange with ethanol, and densification to obtain Zr–*n*$L_4$ ($n$ = 2, 4, 8, and 12; Fig. S57 and S58†). PXRD patterns measured for the resulting material confirmed the retention of its amorphous nature after the modification without forming any crystalline oxide byproduct (Fig. 3B and S59†). Additionally, TGA results revealed that Zr–*n*$L_4$ samples are thermally stable to at least 250 °C and contain 15–17 wt% of interstitial water (Fig. S60–S63†).

Initial evidence of complete thiol oxidation was obtained from FTIR spectra (Fig. 3C and S64–S67†). The S–H band (2556–2561 $cm^{-1}$) was replaced by newly formed bands centred at 1205, 1125, and 1038 $cm^{-1}$, corresponding to $\nu_{as}$(O=S=O), *vs.*(O=S=O), and S–O stretching, respectively.[41,58] Additionally, the post-synthetic modification eliminated non-coordinating carboxylate or carboxylic acid, as C=O stretching at 1690–1730 $cm^{-1}$ disappeared in all samples. Following this confirmation, Zr–4$L_4$ was chosen for further characterisation. XPS confirmed no changes in the oxidation state of $Zr^{4+}$ (Fig. 3D), while the S 2p peaks shifted to a higher binding energy after the oxidation treatment (Fig. 3E), with S $2p_{3/2}$ shifting from 163.4 eV of –SH to 168.8 of –$SO_3H$ in Zr–4$L_3$ and Zr–4$L_4$, respectively.[41,59] The $^1$H NMR of the digested Zr–4$L_4$ confirmed a complete conversion, as evidenced by the shift of the CH peak adjacent to the functional group from 3.50–3.54 ppm in Zr–4$L_3$ (Fig. S35†) to 3.93–3.97 ppm in Zr–4$L_4$ (Fig. S69†). TGA analysis under air indicated a partial linker elimination after the treatment, as the ratio between bidentate ligands and $Zr_6$ clusters decreased to 2.8 in Zr–4$L_4$ (Fig. S70†).

The local structure after post-synthetic modification (Zr–4$L_4$) was analysed through X-ray total scattering (Fig. 3F) and EXAFS (Fig. 3G). PDF data revealed a distortion in the $Zr_6$ node, as evidenced by a shift in the Zr–$Zr_{adj}$ peak from 3.53 Å in Zr–4$L_3$ to 3.49 Å in Zr–4$L_4$, along with the emergence of a peak at 4.0 Å. A minor contraction in the Zr–O distance was also observed, decreasing from 2.21 to 2.18 Å. While the Zr–O, Zr–$Zr_{adj}$, and Zr–$Zr_{opp}$ peaks are retained, their relative intensities are altered. In the FT-EXAFS (Fig. 3G), we observed a decrease in the peak intensities for Zr–$Zr_{opp}$ pairs and a splitting of the Zr–$Zr_{adj}$ peak in Zr–4$L_4$ compared to Zr–4$L_3$. The relative intensity of the Zr–O peak was increased in both PDF and EXAFS results. This is explained by incorporating capping water or hydroxide ions around $Zr^{4+}$ to complete the coordination sphere following partial ligand elimination.[55] Similar node distortions and alterations in PDF peaks have been observed in a series of crystalline NU-1000 MOFs, where varying node capping ligands influenced the extent of ligand elimination during thermal treatment.[60,61] No amorphous $ZrO_2$ or $Zr(OH)_4$ byproducts were observed (Fig. S71†).

Another cause of the node distortion is the coordination of sulfate anions to the outer surface of $Zr_6$ clusters during the protonation step. EXAFS fitting confirmed the incorporation of sulfate anions in Zr–4$L_4$, with the data fitted well to the crystal structure of the $[Zr_6O_4(OH)_4(OH_2)_8(HCOO)_4(SO_4)_4]\cdot 2HCl\cdot 3H_2O$[56] (Fig. 3H, I and Table S2†), showing a reduced Zr–Zr distance of 3.47–3.50 Å. Similar behaviour has been observed in MOF-808 ($Zr_6O_5(OH)_3(BTC)_2(HCOO)_5(OH_2)$, BTC = benzenetricarboxylate), where sulfate anions replaced coordinated formate groups on $Zr_6$ clusters after washing with dilute sulfuric acid.[62,63] These sulfate anions increase node distortion by coordinating with the $Zr_6$ clusters in multiple binding modes.

## Porosity, proton conductivity, and mechanical properties

The influence of the ligand on gas-accessible porosity was investigated *via* $N_2$ physisorption. All samples were activated at 130 °C for 12 h under a dynamic vacuum. At 77 K, Zr–4$L_1$ and Zr–4$L_2$ with aliphatic ligands exhibited negligible $N_2$ adsorption (Fig. S72†). Positron annihilation lifetime spectroscopy (PALS) on Zr–4$L_1$ and Zr–4$L_2$ was used to further probe the free spaces in both samples that are quasi-inaccessible to probe molecules (Fig. S73 and S74†).[35,64] PALS detects free space within materials by measuring the lifetime of *ortho*-positronium (*o*-Ps) when exposed to a $^{22}$Na positron source. The average pore diameter of each sample is calculated from the lifetime of *o*-Ps, with a longer lifetime corresponding to a larger average pore diameter. The *o*-Ps lifetime of Zr–4$L_1$ is 2.90 ± 0.04 ns, corresponding to an average pore diameter of 3.57 ± 0.03 Å. The longer ligand in Zr–4$L_2$ results in a longer *o*-Ps lifetime of 3.71 ± 0.09 ns, translating to a pore diameter of 4.08 ± 0.05 Å. These results confirm the

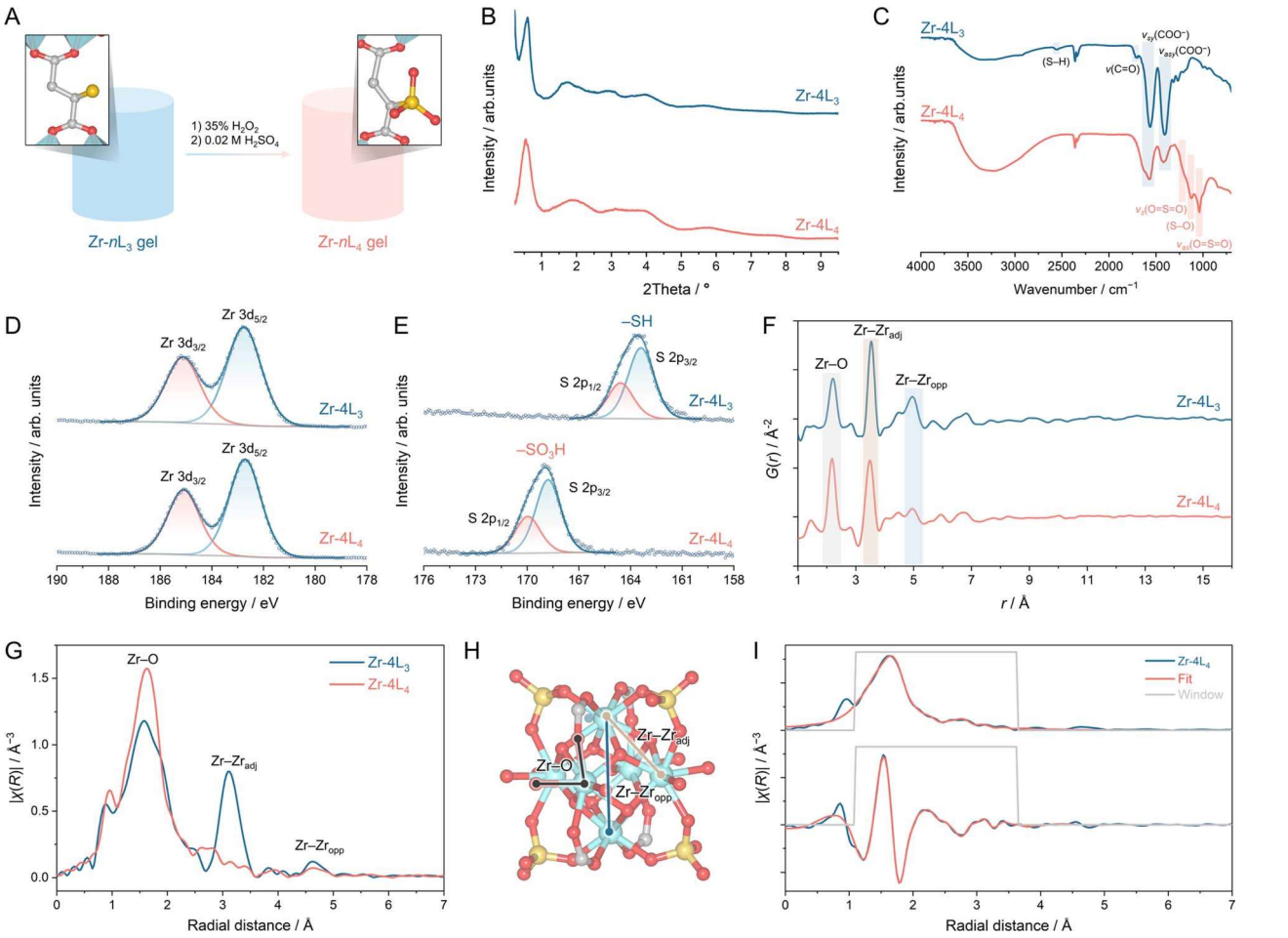


Fig. 3 Post-synthetic modification of cross-linked zirconium-based aMOF. (A) Schematic overview of the oxidation of thiols (–SH) to sulfonic acid groups ($-SO_3H$) in gel phase before densification. (B) Synchrotron powder X-ray diffraction (PXRD, $\lambda = 0.109795$ Å) of Zr–4$L_3$ and Zr–4$L_4$. (C) FTIR spectra of Zr–4$L_3$ and Zr–4$L_4$. XPS spectra at (D) Zr 3d and (E) S 2p of Zr–4$L_3$ and Zr–4$L_4$. (F) PDF and (G) EXAFS at Zr K-edge of Zr–4$L_3$ and Zr–4$L_4$. (H) Model for EXAFS fitting derived from the crystal structure of $[Zr_6O_4(OH)_4(OH_2)_8(HCOO)_4(SO_4)_4]\cdot 2HCl\cdot 3H_2O$,[56] with Zr, C, O, and S atoms represented by light blue, grey, red, and yellow, respectively. (I) Fourier transforms (magnitude and real component) of EXAFS at the Zr K-edge with fitting curves for Zr–4$L_4$. The fitted results are presented in Table S2.†

presence of free spaces in both samples that are large enough to accommodate $N_2$ (3.6 Å) but remain inaccessible.

At 77 K, Zr–4$L_3$ and Zr–4$L_4$ show $N_2$ uptakes of 22.2 and 17.2 $cm^3\ g^{-1}$, respectively (Fig. S72†). The presence of side groups likely introduces steric hindrance, preventing pore collapse and preserving space large enough for $N_2$.[65] While Zr–4$L_3$ displays a type I isotherm characteristic of microporous materials, the type IV isotherm observed in Zr–4$L_4$ further confirms the partial elimination of bidentate linkers and the formation of mesopores following post-synthesis modification.[66]

Promoting proton ($H^+$) conductivity in crystalline MOFs is achievable by increasing the $H^+$ carrier concentration or establishing continuous H-bonding networks.[6,71] However, no example of systematic $H^+$ conductivity control by gradually modifying the structure in aMOF has been demonstrated.[6,13,71,72] We chose Zr–4$L_1$, Zr–4$L_3$, and Zr–4$L_4$, with comparable ligand lengths, to investigate the effects of tethered functional groups in aMOFs on $H^+$ conductivity (Fig. 4A). We measured the $H^+$ conductivity of the aMOFs by variable-temperature alternating current (AC) impedance spectroscopy under a humidified atmosphere (95% RH). The $H^+$ conductivity of Zr–4$L_1$ is $6.7 \times 10^{-3}$ mS $cm^{-1}$ at 30 °C and increases to $8.5 \times 10^{-2}$ mS $cm^{-1}$ at 70 °C. The activation energy for $H^+$ conduction ($E_a$, Fig. S75†) is 0.63 eV. In this case, $H^+$ mainly diffuses through the H-bonding network between interstitial water guest molecules and non-coordinating or protonated carboxylates since the main alkyl chain of the $L_1$ ligand contains no tethered functional groups to act as a hopping site.[6] Note that Zr–4$L_1$ contains *ca.* 10.7 wt% water molecules (Fig. S14†). Zr–4$L_3$ contains weakly acidic thiol (–SH, $pK_a \approx 7.8$) side groups, contributing as an additional hopping site. The $H^+$ conductivity values of $1.7 \times 10^{-2}$ mS $cm^{-1}$ and $9.9 \times 10^{-2}$ mS $cm^{-1}$ were achieved at 30 °C and 70 °C, respectively. Replacing thiols with sulfonic acid groups ($-SO_3H$, $pK_a \approx -1.7$), a strong Brønsted acid site, in Zr–4$L_4$ together with the incorporation of sulfate anion on the surface of the $Zr_6$ clusters further increases the conductivity to $3.1 \times 10^{-2}$ mS $cm^{-1}$ and 0.16 mS $cm^{-1}$ at 30 °C and 70 °C. Sulfonic acid groups also contribute to the hydrophilic character of Zr–4$L_4$,

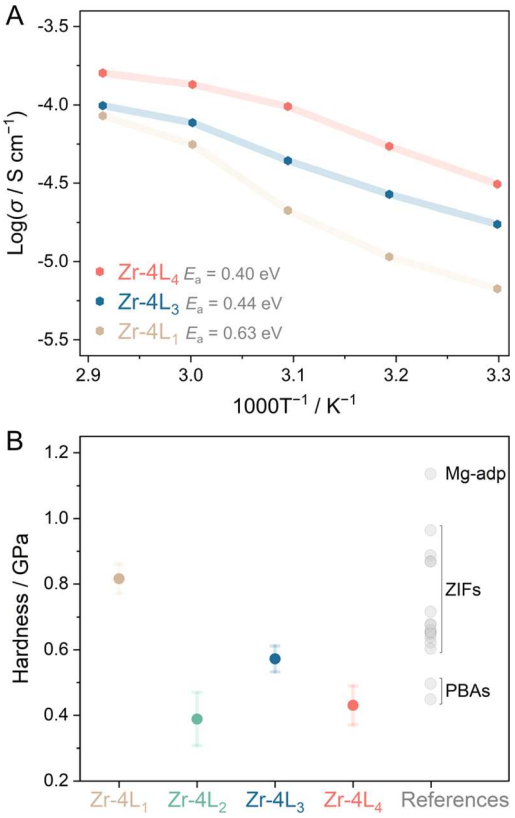


Fig. 4 (A) Variable-temperature $H^+$ conductivity measurements at 95% RH of Zr–$4L_1$, Zr–$4L_3$, and Zr–$4L_4$. The activation energy for $H^+$ conduction was calculated from Arrhenius plots (Fig. S75†). (B) Hardness values obtained with the triangular pyramid nano-indenter with a 115° tip angle of Zr–$4L_1$, Zr–$4L_2$, Zr–$4L_3$, and Zr–$4L_4$. Data points represent mean hardness with 95% confidence intervals. Reference hardness data from other CP/MOF glasses are taken from ref. 40, 45 and 67–70.

with an interstitial water content of 17 wt%. Incorporating functional groups in Zr–$4L_3$ and Zr–$4L_4$ reduced the $E_a$ to 0.44 and 0.40 eV, respectively. The order of $H^+$ conductivity and inverse $E_a$ for proton conduction in this series is Zr–$4L_1$ < Zr–$4L_3$ < Zr–$4L_4$. Thus, the $H^+$ conductivity is controlled *via* the acidity of the side group, even in amorphous forms.

In addition to porosity and $H^+$ conductivity, we investigated the correlation between the choice of ligands and bulk mechanical properties of the aMOFs using nano-indentation equipped with a standard triangular pyramid indenter with a 115° tip angle (Fig. 4B). From load-depth curves, we determined the mean hardness (HT115) for Zr–$4L_1$, Zr–$4L_2$, Zr–$4L_3$, and Zr–$4L_4$ as 0.82, 0.39, 0.57, and 0.43 GPa, respectively. A notable decrease in hardness was observed in Zr–$4L_2$ compared to Zr–$4L_1$, attributed to an increase in ligand length. A similar trend in mechanical properties was also noted in $Zr_6$-based crystalline MOFs when comparing the theoretical average bulk modulus of 40 GPa in UiO-66 with 17.4 GPa in UiO-67 [$Zr_6O_4(OH)_4(bpdc)_6$] (bpdc: 4,4′-biphenyl dicarboxylate), an extended counterpart.[73–75] Beyond ligand length, functional side groups and interstitial molecules also decreased the mechanical hardness, likely due to steric hindrance.[70,75] This hypothesis is supported by increased $N_2$ uptake in Zr–$4L_3$ and Zr–$4L_4$ compared to Zr–$4L_1$ and Zr–$4L_2$. However, a substantial decrease in mechanical modulus is evident when framework connectivity is lowered,[76] elucidating the behaviour observed in Zr–$4L_3$ and node-distorted Zr–$4L_4$.

## Conclusions

We demonstrated a method for systematically designing and synthesising a series of aMOFs by crosslinking a well-defined metal cluster with various flexible carboxylate ligands. After gelation and densification, glass-like monolithic products were formed. Synchrotron X-ray total scattering and EXAFS revealed the preservation of $Zr_6$ cluster units after forming extended networks in all samples, even without long-range ordering. To demonstrate the versatility of our approach, we conducted post-synthetic thiol oxidation to obtain sulfonic and functionalised aMOFs. Finally, we established a correlation between the choice of functional groups, ligand length, porosity, proton conductivity, and mechanical properties. Our results indicate that the properties of aMOFs can be modified in a way comparable to their crystalline counterparts, emphasising the impact of precursor selection. This work thus establishes a foundation for the systematic design of novel amorphous metal–organic hybrid systems.

## Data availability

The data supporting this article are available in the main text and ESI.†

## Author contributions

N. M. and R. A. designed the project. N. M. synthesised, analysed, and characterised samples. S. K., S. H., and N. M. collected and analysed XAFS and PDF data. J. T. carried out NMR measurements. N. G. and T. H. conducted XPS measurements. K. O. conducted gas sorption experiments. The manuscript was written with contributions from all authors. All authors have approved the final version of the manuscript.

## Conflicts of interest

There are no conflicts to declare.

## Acknowledgements

The authors acknowledge the Flemish Research Foundation (FWO Vlaanderen) for support in the EOS research project G0H0522N, KU Leuven for research project C14/20/085, and VLAIO for research project HBC.2021.0580. N. M. acknowledges the support from the Flemish Research Foundation (FWO Vlaanderen) for a Junior Postdoctoral Fellowship (1280924N) and a travel grant for a short stay abroad (K1DE523N), from ICYS for a research fellowship, and from the JSPS KAKENHI Grant Number JP24K23109. S. K. acknowledges the JSPS post-doctoral fellowship. J. T. acknowledges the support from FWO

Vlaanderen and F. R. S.-FNRS under the Excellence of Science (EOS) program of a doctoral fellowship (G0H0522N). We acknowledge BL04B2 beamlines at SPring-8 for the synchrotron X-ray total scattering experiments with the approval of JASRI (Proposal No. 2023B1721). We acknowledge BL14B2 beamlines at SPring-8 for the XAFS measurements (Proposal No. 2023B1750). We acknowledge the NMR core at Hasselt University. We acknowledge the European Synchrotron Radiation Facility (ESRF) for the provision of synchrotron radiation facilities under proposal number CH-6893 (DOI 10.15151/ESRF-ES-1442319021), and we would like to thank Pierre-Olivier Autran for assistance and support in using beamline ID11. We acknowledge Dr Takashi Nakanishi for providing access to PALS measurements. We acknowledge Dr Renzhi Ma for providing access to TGA measurement under air.

## References

1 O. M. Yaghi, M. O'Keeffe, N. W. Ockwig, H. K. Chae, M. Eddaoudi and J. Kim, Reticular synthesis and the design of new materials, *Nature*, 2003, **423**, 705–714.
2 S. Kitagawa, R. Kitaura and S.-i. Noro, Functional Porous Coordination Polymers, *Angew. Chem., Int. Ed.*, 2004, **43**, 2334–2375.
3 S. Horike, S. Shimomura and S. Kitagawa, Soft porous crystals, *Nat. Chem.*, 2009, **1**, 695.
4 N. C. Burtch, H. Jasuja and K. S. Walton, Water Stability and Adsorption in Metal–Organic Frameworks, *Chem. Rev.*, 2014, **114**, 10575–10612.
5 T. Islamoglu, Z. Chen, M. C. Wasson, C. T. Buru, K. O. Kirlikovali, U. Afrin, M. R. Mian and O. K. Farha, Metal–Organic Frameworks against Toxic Chemicals, *Chem. Rev.*, 2020, **120**, 8130–8160.
6 D.-W. Lim and H. Kitagawa, Proton Transport in Metal–Organic Frameworks, *Chem. Rev.*, 2020, **120**, 8416–8467.
7 A. M. Rice, C. R. Martin, V. A. Galitskiy, A. A. Berseneva, G. A. Leith and N. B. Shustova, Photophysics Modulation in Photoswitchable Metal–Organic Frameworks, *Chem. Rev.*, 2020, **120**, 8790–8813.
8 L. S. Xie, G. Skorupskii and M. Dincă, Electrically Conductive Metal–Organic Frameworks, *Chem. Rev.*, 2020, **120**, 8536–8580.
9 H. Jiang, D. Alezi and M. Eddaoudi, A reticular chemistry guide for the design of periodic solids, *Nat. Rev. Mater.*, 2021, **6**, 466–487.
10 S. J. Garibay and S. M. Cohen, Isoreticular synthesis and modification of frameworks with the UiO-66 topology, *Chem. Commun.*, 2010, **46**, 7700–7702.
11 S. M. Cohen, Postsynthetic Methods for the Functionalization of Metal–Organic Frameworks, *Chem. Rev.*, 2012, **112**, 970–1000.
12 S. Horike, N. Ma, Z. Fan, S. Kosasang and M. M. Smedskjaer, Mechanics, Ionics, and Optics of Metal–Organic Framework and Coordination Polymer Glasses, *Nano Lett.*, 2021, **21**, 6382–6390.
13 J. Fonseca, T. Gong, L. Jiao and H.-L. Jiang, Metal-Organic Frameworks (MOFs) beyond Crystallinity: Amorphous MOFs, MOF Liquids and MOF Glasses, *J. Mater. Chem. A*, 2021, **9**, 10562–10611.
14 N. Ma and S. Horike, Metal–Organic Network-Forming Glasses, *Chem. Rev.*, 2022, **122**, 4163–4203.
15 D. Umeyama, S. Horike, M. Inukai, T. Itakura and S. Kitagawa, Reversible Solid-to-Liquid Phase Transition of Coordination Polymer Crystals, *J. Am. Chem. Soc.*, 2015, **137**, 864–870.
16 A. Qiao, H. Tao, M. P. Carson, S. W. Aldrich, L. M. Thirion, T. D. Bennett, J. C. Mauro and Y. Yue, Optical properties of a melt-quenched metal-organic framework glass, *Opt. Lett.*, 2019, **44**, 1623–1625.
17 Y. Wang, H. Jin, Q. Ma, K. Mo, H. Mao, A. Feldhoff, X. Cao, Y. Li, F. Pan and Z. Jiang, A MOF Glass Membrane for Gas Separation, *Angew. Chem., Int. Ed.*, 2020, **59**, 4365–4369.
18 N. Ma, S. Kosasang, A. Yoshida and S. Horike, Proton-conductive coordination polymer glass for solid-state anhydrous proton batteries, *Chem. Sci.*, 2021, **12**, 5818–5824.
19 J. Li, J. Wang, Q. Li, M. Zhang, J. Li, C. Sun, S. Yuan, X. Feng and B. Wang, Coordination Polymer Glasses with Lava and Healing Ability for High-Performance Gas Sieving, *Angew. Chem., Int. Ed.*, 2021, **60**, 21304–21309.
20 Z. Yang, Y. Belmabkhout, L. N. McHugh, D. Ao, Y. Sun, S. Li, Z. Qiao, T. D. Bennett, M. D. Guiver and C. Zhong, ZIF-62 glass foam self-supported membranes to address $CH_4/N_2$ separations, *Nat. Mater.*, 2023, **22**, 888–894.
21 T. D. Bennett, J.-C. Tan, Y. Yue, E. Baxter, C. Ducati, N. J. Terrill, H. H. M. Yeung, Z. Zhou, W. Chen, S. Henke, A. K. Cheetham and G. N. Greaves, Hybrid glasses from strong and fragile metal-organic framework liquids, *Nat. Commun.*, 2015, **6**, 8079.
22 Z. Yin, Y. Zhao, S. Wan, J. Yang, Z. Shi, S.-X. Peng, M.-Z. Chen, T.-Y. Xie, T.-W. Zeng, O. Yamamuro, M. Nirei, H. Akiba, Y.-B. Zhang, H.-B. Yu and M.-H. Zeng, Synergistic Stimulation of Metal–Organic Frameworks for Stable Super-cooled Liquid and Quenched Glass, *J. Am. Chem. Soc.*, 2022, **144**, 13021–13025.
23 Y.-S. Wei, Z. Fan, C. Luo and S. Horike, Desolvation of metal complexes to construct metal–organic framework glasses, *Nat. Synth.*, 2023, **3**, 214–223.
24 W. Chen, S. Horike, D. Umeyama, N. Ogiwara, T. Itakura, C. Tassel, Y. Goto, H. Kageyama and S. Kitagawa, Glass Formation of a Coordination Polymer Crystal for Enhanced Proton Conductivity and Material Flexibility, *Angew. Chem., Int. Ed.*, 2016, **55**, 5195–5200.
25 K. W. Chapman, G. J. Halder and P. J. Chupas, Pressure-Induced Amorphization and Porosity Modification in a Metal–Organic Framework, *J. Am. Chem. Soc.*, 2009, **131**, 17546–17547.
26 K. W. Chapman, D. F. Sava, G. J. Halder, P. J. Chupas and T. M. Nenoff, Trapping Guests within a Nanoporous Metal–Organic Framework through Pressure-Induced Amorphization, *J. Am. Chem. Soc.*, 2011, **133**, 18583–18585.
27 R. N. Widmer, G. I. Lampronti, N. Casati, S. Farsang, T. D. Bennett and S. A. T. Redfern, X-ray radiation-induced amorphization of metal–organic frameworks, *Phys. Chem. Chem. Phys.*, 2019, **21**, 12389–12395.

28 A. M. Bumstead, I. Pakamorė, K. D. Richards, M. F. Thorne, S. S. Boyadjieva, C. Castillo-Blas, L. N. McHugh, A. F. Sapnik, D. S. Keeble, D. A. Keen, R. C. Evans, R. S. Forgan and T. D. Bennett, Post-Synthetic Modification of a Metal–Organic Framework Glass, *Chem. Mater.*, 2022, **34**, 2187–2196.

29 S. Dai, C. Simms, I. Dovgaliuk, G. Patriarche, A. Tissot, T. N. Parac-Vogt and C. Serre, Monodispersed MOF-808 Nanocrystals Synthesized via a Scalable Room-Temperature Approach for Efficient Heterogeneous Peptide Bond Hydrolysis, *Chem. Mater.*, 2021, **33**, 7057–7066.

30 A. V. Zhukhovitskiy, M. Zhong, E. G. Keeler, V. K. Michaelis, J. E. P. Sun, M. J. A. Hore, D. J. Pochan, R. G. Griffin, A. P. Willard and J. A. Johnson, Highly branched and loop-rich gels via formation of metal–organic cages linked by polymers, *Nat. Chem.*, 2016, **8**, 33–41.

31 Y. Gu, E. A. Alt, H. Wang, X. Li, A. P. Willard and J. A. Johnson, Photoswitching topology in polymer networks with metal–organic cages as crosslinks, *Nature*, 2018, **560**, 65–69.

32 A. Carné-Sánchez, G. A. Craig, P. Larpent, T. Hirose, M. Higuchi, S. Kitagawa, K. Matsuda, K. Urayama and S. Furukawa, Self-assembly of metal–organic polyhedra into supramolecular polymers with intrinsic microporosity, *Nat. Commun.*, 2018, **9**, 2506.

33 Z. Wang, C. Villa Santos, A. Legrand, F. Haase, Y. Hara, K. Kanamori, T. Aoyama, K. Urayama, C. M. Doherty, G. J. Smales, B. R. Pauw, Y. J. Colón and S. Furukawa, Multiscale structural control of linked metal–organic polyhedra gel by aging-induced linkage-reorganization, *Chem. Sci.*, 2021, **12**, 12556–12563.

34 A. Khobotov-Bakishev, L. Hernández-López, C. von Baeckmann, J. Albalad, A. Carné-Sánchez and D. Maspoch, Metal–Organic Polyhedra as Building Blocks for Porous Extended Networks, *Adv. Sci.*, 2022, **9**, 2104753.

35 Z. Wang, A. Ozcan, G. A. Craig, F. Haase, T. Aoyama, D. Poloneeva, K. Horio, M. Higuchi, M.-S. Yao, C. M. Doherty, G. Maurin, K. Urayama, A. Bavykina, S. Horike, J. Gascon, R. Semino and S. Furukawa, Pore-Networked Gels: Permanently Porous Ionic Liquid Gels with Linked Metal–Organic Polyhedra Networks, *J. Am. Chem. Soc.*, 2023, **145**, 14456–14465.

36 D. Nam, J. Huh, J. Lee, J. H. Kwak, H. Y. Jeong, K. Choi and W. Choe, Cross-linking Zr-based metal–organic polyhedra via postsynthetic polymerization, *Chem. Sci.*, 2017, **8**, 7765–7771.

37 I. Pappas, M. Fitzgerald, X.-Y. Huang, J. Li and L. Pan, Thermally Resolved in Situ Dynamic Light Scattering Studies of Zirconium(IV) Complex Formation, *Cryst. Growth Des.*, 2009, **9**, 5213–5219.

38 C. Hennig, S. Weiss, W. Kraus, J. Kretzschmar and A. C. Scheinost, Solution Species and Crystal Structure of Zr(IV) Acetate, *Inorg. Chem.*, 2017, **56**, 2473–2480.

39 S. Krishnan, C. J. Raj, R. Robert, A. Ramanand and S. J. Das, Growth and characterization of succinic acid single crystals, *Cryst. Res. Technol.*, 2007, **42**, 1087–1090.

40 M. Kim, H.-S. Lee, D.-H. Seo, S. J. Cho, E.-c. Jeon and H. R. Moon, Melt-quenched carboxylate metal–organic framework glasses, *Nat. Commun.*, 2024, **15**, 1174.

41 W. J. Phang, H. Jo, W. R. Lee, J. H. Song, K. Yoo, B. Kim and C. S. Hong, Superprotonic Conductivity of a UiO-66 Framework Functionalized with Sulfonic Acid Groups by Facile Postsynthetic Oxidation, *Angew. Chem., Int. Ed.*, 2015, **54**, 5142–5146.

42 A. Kundu, S. K. Barman and S. Mandal, Dangling Carboxylic Group That Participates in O–O Bond Formation Reaction to Promote Water Oxidation Catalyzed by a Ruthenium Complex: Experimental Evidence of an Oxide Relay Pathway, *Inorg. Chem.*, 2022, **61**, 1426–1437.

43 L. Valenzano, B. Civalleri, S. Chavan, S. Bordiga, M. H. Nilsen, S. Jakobsen, K. P. Lillerud and C. Lamberti, Disclosing the Complex Structure of UiO-66 Metal Organic Framework: A Synergic Combination of Experiment and Theory, *Chem. Mater.*, 2011, **23**, 1700–1718.

44 Q. Zheng, Y. Zhang, M. Montazerian, O. Gulbiten, J. C. Mauro, E. D. Zanotto and Y. Yue, Understanding Glass through Differential Scanning Calorimetry, *Chem. Rev.*, 2019, **119**, 7848–7939.

45 T. D. Bennett, Y. Yue, P. Li, A. Qiao, H. Tao, N. G. Greaves, T. Richards, G. I. Lampronti, S. A. T. Redfern, F. Blanc, O. K. Farha, J. T. Hupp, A. K. Cheetham and D. A. Keen, Melt-Quenched Glasses of Metal–Organic Frameworks, *J. Am. Chem. Soc.*, 2016, **138**, 3484–3492.

46 N. Ma, N. Horike, L. Lombardo, S. Kosasang, K. Kageyama, C. Thanaphatkosol, K. Kongpatpanich, K.-i. Otake and S. Horike, Eutectic $CsHSO_4$-Coordination Polymer Glasses with Superprotonic Conductivity, *J. Am. Chem. Soc.*, 2022, **144**, 18619–18628.

47 T. E. Faber and J. M. Ziman, A theory of the electrical properties of liquid metals, *Philos. Mag.*, 1965, **11**, 153–173.

48 E. Lorch, Neutron diffraction by germania, silica and radiation-damaged silica glasses, *J. Phys. C: Solid State Phys.*, 1969, **2**, 229–237.

49 S. Kohara, M. Itou, K. Suzuya, Y. Inamura, Y. Sakurai, Y. Ohishi and M. Takata, Structural studies of disordered materials using high-energy x-ray diffraction from ambient to extreme conditions, *J. Phys. Condens. Matter*, 2007, **19**, 506101.

50 H. Furukawa, F. Gándara, Y.-B. Zhang, J. Jiang, W. L. Queen, M. R. Hudson and O. M. Yaghi, Water Adsorption in Porous Metal–Organic Frameworks and Related Materials, *J. Am. Chem. Soc.*, 2014, **136**, 4369–4381.

51 S. Wang, M. Wahiduzzaman, L. Davis, A. Tissot, W. Shepard, J. Marrot, C. Martineau-Corcos, D. Hamdane, G. Maurin, S. Devautour-Vinot and C. Serre, A robust zirconium amino acid metal-organic framework for proton conduction, *Nat. Commun.*, 2018, **9**, 4937.

52 D. A. Keen and A. L. Goodwin, The crystallography of correlated disorder, *Nature*, 2015, **521**, 303–309.

53 T. T. Y. Tan, X. Li, K.-i. Otake, Y. C. Tan, X. J. Loh, S. Kitagawa and J. Y. C. Lim, UiO-66 metal organic frameworks with high contents of flexible adipic acid co-linkers, *Chem. Commun.*, 2022, **58**, 11402–11405.

54 L. Pan, R. Heddy, J. Li, C. Zheng, X.-Y. Huang, X. Tang and L. Kilpatrick, Synthesis and Structural Determination of a Hexanuclear Zirconium Glycine Compound Formed in Aqueous Solution, *Inorg. Chem.*, 2008, **47**, 5537–5539.

55 C. A. Trickett, K. J. Gagnon, S. Lee, F. Gándara, H.-B. Bürgi and O. M. Yaghi, Definitive Molecular Level Characterization of Defects in UiO-66 Crystals, *Angew. Chem., Int. Ed.*, 2015, **54**, 11162–11167.

56 Q. Sun, C. Liu, G. Zhang, J. Zhang, C.-H. Tung and Y. Wang, Aqueous Isolation of 17-Nuclear Zr/Hf Oxide Clusters during the Hydrothermal Synthesis of $ZrO_2$/$HfO_2$, *Chem.–Eur. J.*, 2018, **24**, 14701–14706.

57 L. A. H. van Bergen, G. Roos and F. De Proft, From Thiol to Sulfonic Acid: Modeling the Oxidation Pathway of Protein Thiols by Hydrogen Peroxide, *J. Phys. Chem. A*, 2014, **118**, 6078–6084.

58 K. I. Hadjiivanov, D. A. Panayotov, M. Y. Mihaylov, E. Z. Ivanova, K. K. Chakarova, S. M. Andonova and N. L. Drenchev, Power of Infrared and Raman Spectroscopies to Characterize Metal-Organic Frameworks and Investigate Their Interaction with Guest Molecules, *Chem. Rev.*, 2020, **121**, 1286–1424.

59 Y. Zhou, R. Huang, F. Ding, A. D. Brittain, J. Liu, M. Zhang, M. Xiao, Y. Meng and L. Sun, Sulfonic Acid-Functionalized α-Zirconium Phosphate Single-Layer Nanosheets as a Strong Solid Acid for Heterogeneous Catalysis Applications, *ACS Appl. Mater. Interfaces*, 2014, **6**, 7417–7425.

60 A. E. Platero-Prats, A. Mavrandonakis, L. C. Gallington, Y. Liu, J. T. Hupp, O. K. Farha, C. J. Cramer and K. W. Chapman, Structural Transitions of the Metal-Oxide Nodes within Metal–Organic Frameworks: On the Local Structures of NU-1000 and UiO-66, *J. Am. Chem. Soc.*, 2016, **138**, 4178–4185.

61 Z. Chen, G. D. Stroscio, J. Liu, Z. Lu, J. T. Hupp, L. Gagliardi and K. W. Chapman, Node Distortion as a Tunable Mechanism for Negative Thermal Expansion in Metal–Organic Frameworks, *J. Am. Chem. Soc.*, 2023, **145**, 268–276.

62 J. Jiang, F. Gándara, Y.-B. Zhang, K. Na, O. M. Yaghi and W. G. Klemperer, Superacidity in Sulfated Metal–Organic Framework-808, *J. Am. Chem. Soc.*, 2014, **136**, 12844–12847.

63 C. A. Trickett, T. M. Osborn Popp, J. Su, C. Yan, J. Weisberg, A. Huq, P. Urban, J. Jiang, M. J. Kalmutzki, Q. Liu, J. Baek, M. P. Head-Gordon, G. A. Somorjai, J. A. Reimer and O. M. Yaghi, Identification of the strong Brønsted acid site in a metal–organic framework solid acid catalyst, *Nat. Chem.*, 2019, **11**, 170–176.

64 L. Ma, C. J. E. Haynes, A. B. Grommet, A. Walczak, C. C. Parkins, C. M. Doherty, L. Longley, A. Tron, A. R. Stefankiewicz, T. D. Bennett and J. R. Nitschke, Coordination cages as permanently porous ionic liquids, *Nat. Chem.*, 2020, **12**, 270–275.

65 P. M. Budd, B. S. Ghanem, S. Makhseed, N. B. McKeown, K. J. Msayib and C. E. Tattershall, Polymers of intrinsic microporosity (PIMs): robust, solution-processable, organic nanoporous materials, *Chem. Commun.*, 2004, 230–231.

66 Y. Kim, T. Yang, G. Yun, M. B. Ghasemian, J. Koo, E. Lee, S. J. Cho and K. Kim, Hydrolytic Transformation of Microporous Metal–Organic Frameworks to Hierarchical Micro- and Mesoporous MOFs, *Angew. Chem., Int. Ed.*, 2015, **54**, 13273–13278.

67 S. Li, R. Limbach, L. Longley, A. A. Shirzadi, J. C. Walmsley, D. N. Johnstone, P. A. Midgley, L. Wondraczek and T. D. Bennett, Mechanical Properties and Processing Techniques of Bulk Metal–Organic Framework Glasses, *J. Am. Chem. Soc.*, 2019, **141**, 1027–1034.

68 M. Stepniewska, K. Januchta, C. Zhou, A. Qiao, M. M. Smedskjaer and Y. Yue, Observation of indentation-induced shear bands in a metal–organic framework glass, *Proc. Natl. Acad. Sci. U. S. A.*, 2020, **117**, 10149–10154.

69 A. Qiao, T. To, M. Stepniewska, H. Tao, L. Calvez, X. Zhang, M. M. Smedskjaer and Y. Yue, Deformation mechanism of a metal–organic framework glass under indentation, *Phys. Chem. Chem. Phys.*, 2021, **23**, 16923–16931.

70 N. Ma, R. Ohtani, H. M. Le, S. S. Sørensen, R. Ishikawa, S. Kawata, S. Bureekaew, S. Kosasang, Y. Kawazoe, K. Ohara, M. M. Smedskjaer and S. Horike, Exploration of glassy state in Prussian blue analogues, *Nat. Commun.*, 2022, **13**, 4023.

71 P. Ramaswamy, N. E. Wong and G. K. H. Shimizu, MOFs as proton conductors – challenges and opportunities, *Chem. Soc. Rev.*, 2014, **43**, 5913–5932.

72 D.-W. Lim and H. Kitagawa, Rational strategies for proton-conductive metal–organic frameworks, *Chem. Soc. Rev.*, 2021, **50**, 6349–6368.

73 H. Wu, T. Yildirim and W. Zhou, Exceptional Mechanical Stability of Highly Porous Zirconium Metal–Organic Framework UiO-66 and Its Important Implications, *J. Phys. Chem. Lett.*, 2013, **4**, 925–930.

74 C. L. Hobday, R. J. Marshall, C. F. Murphie, J. Sotelo, T. Richards, D. R. Allan, T. Düren, F.-X. Coudert, R. S. Forgan, C. A. Morrison, S. A. Moggach and T. D. Bennett, A Computational and Experimental Approach Linking Disorder, High-Pressure Behavior, and Mechanical Properties in UiO Frameworks, *Angew. Chem., Int. Ed.*, 2016, **55**, 2401–2405.

75 P. G. Yot, K. Yang, F. Ragon, V. Dmitriev, T. Devic, P. Horcajada, C. Serre and G. Maurin, Exploration of the mechanical behavior of metal organic frameworks UiO-66(Zr) and MIL-125(Ti) and their NH2 functionalized versions, *Dalton Trans.*, 2016, **45**, 4283–4288.

76 A. W. Thornton, R. Babarao, A. Jain, F. Trousselet and F. X. Coudert, Defects in metal–organic frameworks: a compromise between adsorption and stability?, *Dalton Trans.*, 2016, **45**, 4352–4359.